Galaxy cluster photons alter the ionization state of the nearby warm-hot intergalactic medium

Štofanová, L.; Simionescu, A.; Wijers, N.A.; Schaye, J.; Kaastra, J.S.

Galaxy cluster photons alter the ionization state of the nearby warm–hot intergalactic medium

Lýdia Štofanová [1,2]★ Aurora Simionescu [1,2,3] Nastasha A. Wijers [1,4] Joop Schaye [1]
and Jelle S. Kaastra [1,2]

[1]*Leiden Observatory, Leiden University, PO Box 9513, NL-2300 RA Leiden, the Netherlands*
[2]*SRON Netherlands Institute for Space Research, Sorbonnelaan 2, NL-3584 CA Utrecht, the Netherlands*
[3]*Kavli Institute for the Physics and Mathematics of the Universe (WPI), The University of Tokyo, Kashiwa, Chiba 277-8583, Japan*
[4]*Center for Interdisciplinary Exploration and Research in Astrophysics (CIERA) and Department of Physics and Astronomy, Northwestern University, 1800 Sherman Avenue, Evanston, IL 60201, USA*

ABSTRACT

The physical properties of the faint and extremely tenuous plasma in the far outskirts of galaxy clusters, the circumgalactic media of normal galaxies, and filaments of the cosmic web remain one of the biggest unknowns in our story of large-scale structure evolution. Modelling the spectral features due to emission and absorption from this very diffuse plasma poses a challenge, as both collisional and photoionization processes must be accounted for. In this paper, we study the ionization by photons emitted by the intracluster medium in addition to the photoionization by the cosmic ultraviolet/X-ray background on gas in the vicinity of galaxy clusters. For near-massive clusters such as A2029, the ionization parameter can no longer describe the ionization balance uniquely. The ionization fractions (in particular of C IV, C V, C VI, N VII, O VI, O VII, O VIII, Ne VIII, Ne IX, and Fe XVII) obtained by taking into account the photoionization by the cosmic background are either an upper or lower limit to the ionization fraction calculated as a function of distance from the emission from the cluster. Using a toy model of a cosmic web filament, we predict how the cluster illumination changes the column densities for two different orientations of the line of sight. For lines of sight passing close to the cluster outskirts, O VI can be suppressed by a factor of up to 4.5, O VII by a factor of 2.2, C V by a factor of 3, and Ne VIII can be boosted by a factor of 2, for low-density gas.

Key words: galaxies: clusters: general – galaxies: intergalactic medium – galaxies: quasars: absorption lines – cosmology: large-scale structure of Universe – X-rays: galaxies: clusters.

1 INTRODUCTION

For almost three decades, scientists have been trying to find the 'missing baryons' in the Universe. The 'missing baryon' problem originates from the comparison of the amount of baryons detected in the high-redshift Universe ($z > 2$) with the amount detected in the local Universe from $z = 0$ to $z = 1$–2. At redshift $z > 2$, these baryons reside in much cooler gas and can predominantly be detected in the so-called Lyman α forest (e.g. Lynds 1971; Sargent et al. 1980; Cen et al. 1994; Zhang, Anninos & Norman 1995; Weinberg et al. 1997; Schaye 2001). To predict where to find them in the local Universe, one needs to rely on cosmological hydrodynamical simulations (e.g. Bristow & Phillipps 1994; Cen & Ostriker 1999), which show that baryons are heated to higher temperatures, mainly via shock heating due to the gravitational collapse and the hierarchical growth of structures in the Universe. In addition, processes such as supernova feedback, active galactic nuclei feedback, radiative cooling, or photoionization can heat up this gas (e.g. Tepper-García et al. 2012). Most of the diffuse baryons in the present epoch have not yet been converted into stars and can be found in groups of galaxies – intragroup medium, in the haloes of galaxy clusters – intracluster medium (ICM), or in the space between them – intergalactic medium (IGM). A subset of the IGM is the warm–hot intergalactic medium (WHIM) permeating large-scale structure filaments, while another component of the IGM consists of gas found in the haloes of galaxies – the so-called circumgalactic medium (CGM).

In this work, we focus on the WHIM, which at low redshift contains around 30–60 per cent of all baryons of the Universe (e.g. Fukugita, Hogan & Peebles 1998; Davé et al. 2001; Shull, Smith & Danforth 2012; Tepper-García et al. 2012; Martizzi et al. 2019; Tuominen et al. 2021). These baryons reside predominantly in the filamentary structures of the cosmic web (e.g. Martizzi et al. 2019; Tuominen et al. 2021) and can be detected mostly in the ultraviolet (UV; see e.g. Nicastro et al. 2003) and X-ray wavebands/energies (e.g. Hellsten, Gnedin & Miralda-Escudé 1998; Fang, Bryan & Canizares 2002a; Wijers et al. 2019; Wijers & Schaye 2021) because of its relatively high temperatures of 10^5–10^7 K. Due to its high temperatures, low electron densities (10^{-6} to 10^{-4} cm^{-3}), and high ionization state, the observations of this very diffuse and tenuous gas are extremely challenging with currently available UV and X-ray missions. Since the emission decreases as density squared and absorption decreases linearly with density, it is more feasible to detect the WHIM in absorption against very bright, point-like sources (e.g. quasars).

★ E-mail: stofanova@strw.leidenuniv.nl

Since oxygen is the most abundant element after hydrogen and helium in Universe, it is common to look for the WHIM gas in O VII and O VIII absorbers, but also in Ne IX or N VII (e.g. Perna & Loeb 1998; Fang, Sembach & Canizares 2003; Rasmussen, Kahn & Paerels 2003; Fujimoto et al. 2004; Nicastro et al. 2005b, 2018; Takei et al. 2007; Ahoranta et al. 2021). Observations of the WHIM in emission, however, are possible, though mostly through stacking methods to obtain higher signal-to-noise ratio to distinguish the WHIM detection from the background. Since we focus on absorption studies in this paper, we only list few of the publications regarding the emission studies (e.g. Kull & Böhringer 1999; Zappacosta et al. 2002; Finoguenov, Briel & Henry 2003; Kaastra et al. 2003; Werner et al. 2008). The IGM can also be detected in the UV. Typical UV absorbers are coming particularly from warm CGM and can be observed in e.g. O VI, C IV, N V, or Ne VI (see e.g. Tumlinson et al. 2011; Werk et al. 2014). For more details, we refer to the CGM review paper by Tumlinson, Peeples & Werk (2017).

The WHIM gas is typically modelled with collisional ionization equilibrium (CIE) models (assuming the gas has only one temperature) and with photoionization models that take into account the photoionizaton by the UV and X-ray background (e.g. Nicastro et al. 2005a). The sources of this background are known to include star-forming galaxies and quasars. The modelling of this background can be very complex and has been described in many previous works, including e.g. Haardt & Madau (2012) and Faucher-Giguère (2020).

The presence of the photoionizing radiation causes a suppression of the cooling rates in comparison with the CIE case. In a CIE plasma, the lighter elements such as hydrogen, carbon, and helium are the dominant coolants for temperatures below $\sim 10^{-2}$ keV (for a plasma with roughly proto-solar metallicities). In highly photoionized gas, these elements are significantly less efficient coolants. The relative contributions of different coolants to the total cooling rate, however, also depend strongly on the shape of the spectrum of the ionizing source. The suppression of cooling rates in photoionized plasma leads to longer cooling times and can affect star/galaxy formation over time. This has been already noted by e.g. Silk (1985), Dekel & Rees (1987), and Babul & White (1991), which show how quasars can ionize the gas in their surroundings and inhibit the formation of galaxies in their neighbourhood. This can propagate through time and even affect the large-scale structure seen in the galaxy distribution. This was also shown in Efstathiou (1992) for the gas of primordial composition (H and He plasma) where the paper explores how the presence of photoionization caused by the extragalactic UV background can inhibit the formation of dwarf galaxies, most prominently in the gas temperature range 10^4–10^5 K (see also Quinn, Katz & Efstathiou 1996; Thoul & Weinberg 1996). Wiersma, Schaye & Smith (2009) showed how UV/X-ray radiation from galaxies and quasars can significantly suppress the cooling rates for gas enriched with metals as well and how this affects the gas with temperatures even up to 10^7 K.

In this paper, we explore how an additional source of photoionization, in this case caused by the photons originating in galaxy clusters in addition to the photoionization by cosmic UV and X-ray background, can change the ionization balance of the WHIM. In Section 2, we model the spectral energy distribution of three different cool-core galaxy clusters together with the cosmic UV/X-ray background, which serves as the ionization source to the photoionization model. In Section 3.1, we describe the main changes to the ionization state of the WHIM by focusing on the most massive galaxy cluster in our sample. We make the comparison to the other two, less massive clusters in Section 3.2. In Section 4.1, we use a simplified model of a filament and predict column densities in

two different orientations: perpendicular and parallel to the line of sight, and provide a comparison to the column densities calculated for the photoionization by the cosmic UV/X-ray background only. In Section 4.2, we show how the cooling rates of the WHIM can be affected by an additional source of photoionization from the galaxy cluster. And finally, Section 5 summarizes our main conclusions. Throughout the paper, we assume a cosmology with total matter density $\Omega_m = 0.3$, dark energy density $\Omega_\Lambda = 0.7$, radiation density $\Omega_r = 0$, curvature $\Omega_k = 0$, and Hubble constant $H_0 = 70 \, \text{km s}^{-1} \, \text{Mpc}^{-1}$.

2 METHODS

2.1 Galaxy cluster selection

For the purpose of our study, we select three relaxed cool-core clusters with different masses and temperatures (A262, A1795, and A2029). We chose these clusters to estimate the effect of the cluster emission on its surrounding medium for a range of cluster parameters. We summarize the main properties of these clusters as reported by Vikhlinin et al. (2006) in Table 1: redshift z, radius r_{500},[1] and observational average temperature T_{spec}, which is obtained from the single-temperature fit to the cluster spectrum (without the central 70 kpc region).

2.2 Density and temperature profiles

Density and temperature profiles for the galaxy cluster sample used in our study are taken from Vikhlinin et al. (2006). The emission measure profile $n_p n_e(r)$ follows

$$n_p n_e(r) = n_0^2 \frac{(r/r_c)^{-\alpha}}{\left(1 + r^2/r_c^2\right)^{3\beta - \alpha/2}} \frac{1}{\left(1 + r^\gamma/r_s^\gamma\right)^{\epsilon/\gamma}} + \frac{n_{02}^2}{\left(1 + r^2/r_{c2}^2\right)^{3\beta_2}}, \quad (1)$$

where n_p and n_e are the proton and electron number density, respectively. Parameters n_0, r_c, r_s, α, β, ϵ, n_{02}, r_{c2}, and β_2 are taken from table 2 in Vikhlinin et al. (2006) and $\gamma = 3$.

The temperature profile $T_{3D}(r)$ is expressed as a product of $t_{\text{cool}}(r)$ and $t(r)$

$$T_{3D}(r) = T_0 \times t_{\text{cool}}(r) \times t(r), \quad (2)$$

where

$$t_{\text{cool}}(r) = \frac{\left(\frac{r}{r_{\text{cool}}}\right)^{a_{\text{cool}}} + \frac{T_{\text{min}}}{T_0}}{\left(\frac{r}{r_{\text{cool}}}\right)^{a_{\text{cool}}} + 1},$$

$$t(r) = \frac{(r/r_t)^{-a}}{\left[1 + \left(\frac{r}{r_t}\right)^b\right]^{c/b}}. \quad (3)$$

Table 1. Redshift z, r_{500}, and T_{spec} of the clusters used in our study taken from Vikhlinin et al. (2006).

Cluster	z	r_{500} (kpc)	T_{spec} (keV)
A262	0.0162	650 ± 21	2.08 ± 0.06
A1795	0.0622	1235 ± 36	6.12 ± 0.05
A2029	0.0779	1362 ± 43	8.47 ± 0.09

---

[1] r_{500} denotes the radius of a sphere within which the mean overdensity is 500 times the critical density of the Universe.

Parameters T_0, r_t, a, b, c, $T_{\min}$, r_{cool}, and a_{cool} for individual clusters are taken from table 3 of Vikhlinin et al. (2006). Both the emission measure profile and the temperature profile as defined by equations (1) and (2), respectively, are three-dimensional.

2.3 SPEX

In this study, we use the SPEctral X-ray and EUV (SPEX) software package (Kaastra, Mewe & Nieuwenhuijzen 1996; Kaastra et al. 2018, 2020) v. 3.06,[2] which is used for modelling and analysis of high-resolution X-ray spectra. With its own atomic data base SPEXACT (The SPEX Atomic Code & Tables), it includes around 4.2×10^6 lines from 30 different chemical elements (H to Zn). More specifically, we use a model for collisional ionization equilibrium *cie* and the *pion* model for photoionization equilibrium (described in Mehdipour, Kaastra & Kallman 2016, for the most recent updates see Štofanová et al. 2021). Unless stated otherwise, we use the protosolar abundances by Lodders, Palme & Gail (2009) and assume that the ICM has solar metallicities.[3]

2.4 Total photon flux seen by an absorbing particle

To calculate spectra of selected clusters, we treat them as extended sources. The clusters are divided into radial bins while setting the outermost radius to r_{500} (we checked that the contribution to the cluster flux from $r_{500} < r < r_{200}$ is small in comparison with $r < r_{500}$). For the integration, we use the QUAD function from the SCIPY library (Virtanen et al. 2020), where the number of shells is set using an adaptive algorithm.[4] For each shell at distance r, we calculate the density and temperature following equations (1) and (2), respectively. Knowing the temperature of each shell, we simulate the spectrum of the shell with the collisional ionization equilibrium (CIE) model in SPEX. The normalization in SPEX is defined as the emission measure $\text{EM} = n_e n_H V$, where V is the volume of the CIE source. Each CIE model is then renormalized by $n_p n_e$ following equation (1).

We estimate the photon flux seen by any absorbing particle for a set of distances R_{abs} between r_{500} and 13 Mpc (for distances greater than 13 Mpc, cluster emission is negligible in comparison with the cosmic UV/X-ray background). The photon flux contribution of the infinitesimally small cluster shell (with a thickness dr) to the total photon flux can be written as the surface integral:

$$\frac{\mathrm{d}F_{\text{shell}}^{\text{ph}}}{\mathrm{d}r} = \iint \frac{\varepsilon_r}{4\pi \, (R_{\text{abs}} - r)^2} \, r^2 \sin\theta \, \mathrm{d}\theta \, \mathrm{d}\varphi \ , \tag{4}$$

where r is a vector from the cluster centre to the cluster shell and R_{abs} is the vector from the centre of the cluster to the absorbing particle. ε_r is the photon specific emissivity at given r. If we rewrite equation (4)

---

[2]For the most recent version, see https://spex-xray.github.io/spex-help/changelog.html.

[3]In practice, the contribution from line emission is subdominant to the bremsstrahlung continuum for the sources we study in this paper (hot and massive galaxy clusters, for which most of the emission comes from cluster cores).

[4]This algorithm sets by default the upper bound of the number of subintervals in each integration step to 50. The algorithm is described in detail at https://docs.scipy.org/doc/scipy/reference/generated/scipy.integrate.quad.html. We checked the integration for higher as well as lower number of subintervals and the change in comparison with the default number of 50 subintervals is negligible (relative differences of the order of 10^{-4} and lower for the comparison between 50 and 10 subintervals).
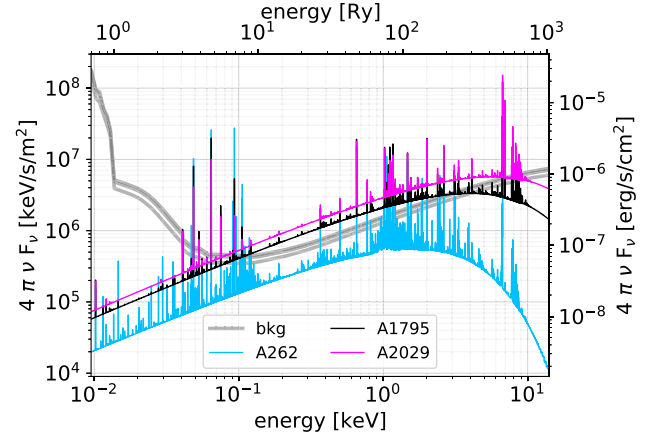
Figure 1. Spectra of the intracluster media of A262 (blue), A1795 (black), and A2029 (pink) and the corresponding cosmic UV/X-ray background at the cluster redshift (grey) as calculated by Faucher-Giguère (2020). We plot spectra for all clusters at a distance of $2 \times r_{500}$. The galaxy cluster spectra are treated as extended sources and their spectrum is a result of summation of CIE models of different temperatures (see the main text for more details).

by defining $L_{\text{shell}} = \varepsilon_r \, 4\pi r^2 \, \mathrm{d}r$, the integral has an analytic solution given by

$$F_{\text{shell}}^{\text{ph}} = \frac{1}{8\pi r \, R_{\text{abs}}} L_{\text{shell}}(r) \ln \left(\frac{R_{\text{abs}} + r}{R_{\text{abs}} - r} \right) \ , \tag{5}$$

which holds for $R_{\text{abs}} > r$. The total photon flux seen by an absorbing particle placed at distance R_{abs} from the galaxy cluster centre is then the integral of equation (5) over radius r from zero to r_{500}.

The spectra of individual clusters are shown in Fig. 1 for A262 (blue), A1795 (black), and A2029 (magenta) at a distance of $2 \times r_{500}$. To account for the effect of photoionization by unresolved background sources, we add the cosmic UV/X-ray background to the spectrum of the cluster. We use the model presented by Faucher-Giguère (2020) (hereafter referred to as *bkg*). For the redshifts of the cluster sample presented in this paper, the background does not differ much. Therefore, we plot all three profiles for the background in Fig. 1 in grey. The final spectrum that we use as an ionizing background in our calculations is then the sum of the cluster spectrum and the cosmic UV/X-ray background.

2.5 Photoionization model

To model the effect of the galaxy cluster emission on the absorbing medium in its vicinity, we assume the medium is in ionization equilibrium, accounting for collisional ionization and photoionization. We describe this plasma with the photoionization model *pion*.

In photoionized plasmas, it is common to define the ionization parameter ξ (Tarter, Tucker & Salpeter 1969; Krolik, McKee & Tarter 1981) as

$$\xi \equiv \frac{L_{1\text{–}1000\,\text{Ry}}}{n_H R_{\text{abs}}^2} \ , \tag{6}$$

where the ionizing source is described by the luminosity $L_{1\text{–}1000\,\text{Ry}}$ over the energy band 1–1000 Ry ($\approx 1.36 \times 10^{-2}$ to 13.6 keV), n_H is the hydrogen number density of a photoionized plasma, and R_{abs} is the distance of the photoionized plasma to the source of ionization.

It is common to tabulate ionization fractions as a function of temperature and the ionization parameter ξ. However, in the model that we are describing in this paper, this does not suffice. The reason is that the shape of the spectrum changes with the distance, because

the relative contributions of different cluster shells and the relative contribution of the background all depend on the distance. This means that the ionization balance can no longer be described solely as a function of ξ and temperature, but it needs to be described as a function of n_H, R_{abs}, and temperature.

To account for this effect, we calculate ξ based on a prescribed array of densities n_H and distances R_{abs} while taking into account the 'correct' shape of the spectrum for each of these distances as described in Section 2.4. For that, we select 30 points for n_H and 30 points for R_{abs}, which are evenly distributed on a logarithmic scale. Densities n_H range from 10^{-6} to 10^{-1} cm^{-3} and R_{abs} goes from r_{500} to approximately 13 Mpc.

In this paper, we use the *pion* model in its temperature mode, which allows us to assume a range of temperatures for the photoionized plasma. This, however, means that instead of solving the ionization balance and the energy balance equations simultaneously, we only solve the ionization balance equation. The consequence of this is that although we assume ionization equilibrium, the plasma is allowed to be out of thermal equilibrium and the equilibrium temperature is only one of the temperatures in the range of the temperatures we used in our studies. This is reasonable for the gas we are probing, since this gas is shock heated and tends to be out of thermal equilibrium because of its long cooling times. For our studies, we select 15 different temperatures in the range 10^{-3} to 1 keV ($\sim 10^4$–10^7 K) evenly distributed on a logarithmic scale.

3 RESULTS

To demonstrate the effect of the additional source of photoionization other than the cosmic UV and X-ray background, in Section 3.1 we focus on the case of the cluster A2029. This cluster has the highest luminosity and alters the ionization balance the most out of all selected clusters. In Section 3.2, we show the comparison of A2029 to the less massive and less hot clusters A1795 and A262.

While we calculated the effect of the cluster emission for the entire grid of electron density, temperature, and R_{abs} as described in Section 2.5, for illustration purposes we present here our results for a limited, representative subset of these parameters.

3.1 A2029

3.1.1 The effect of the cluster emission on the total photoionization and ionization rates

The top panel of Fig. 2 shows the total ionization rate for the background spectral energy distribution (SED) in comparison to that for the A2029 + *bkg* SED as a function of temperature. The total ionization rates are shown for the example of a hydrogen number density of 2.4×10^{-5} cm^{-3} at a distance $2 \times r_{500}$ of the photoionized gas from the galaxy cluster centre. The bottom panel of Fig. 2 shows the ratio of solid and dash–dotted lines in the top panel but for the example set of X-ray and UV ions: C IV, C V, C VI, N V, N VII, O VI, O VII, O VIII, Ne VIII, Ne IX, and Fe XVII. We note that the total ionization and photoionization rates are defined as number of ionizations/photoionizations per second per ion.
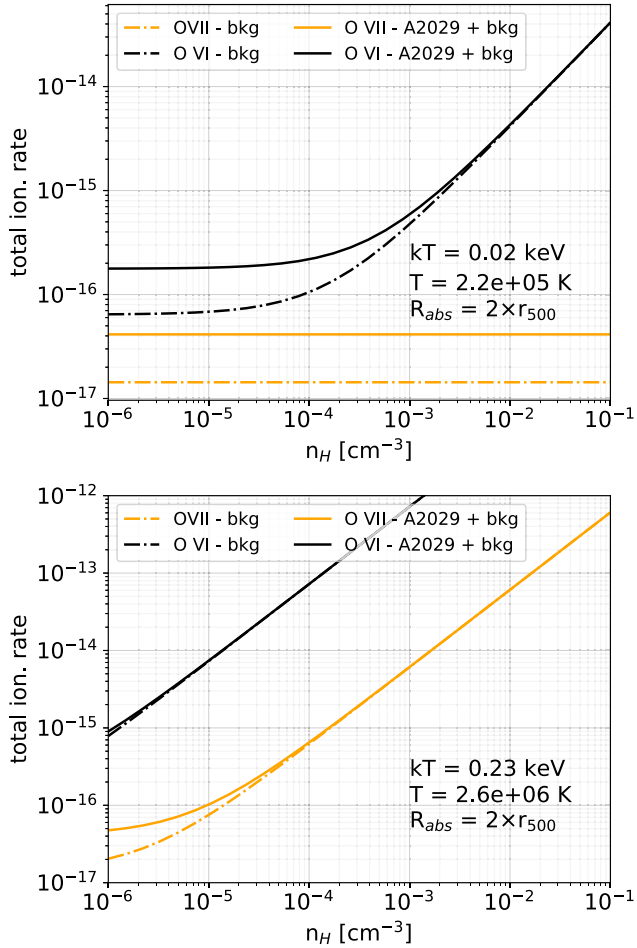
We can see from the plot that for low temperatures (below 20 eV for O VI and below 90 eV for O VII) photoionization is the dominant ionization process. The addition of the cluster emission increases both the ionization and the photoionization rate. However, above a specific ion-dependent temperature, the plasma starts to be dominated by collisions with free electrons and the contribution of
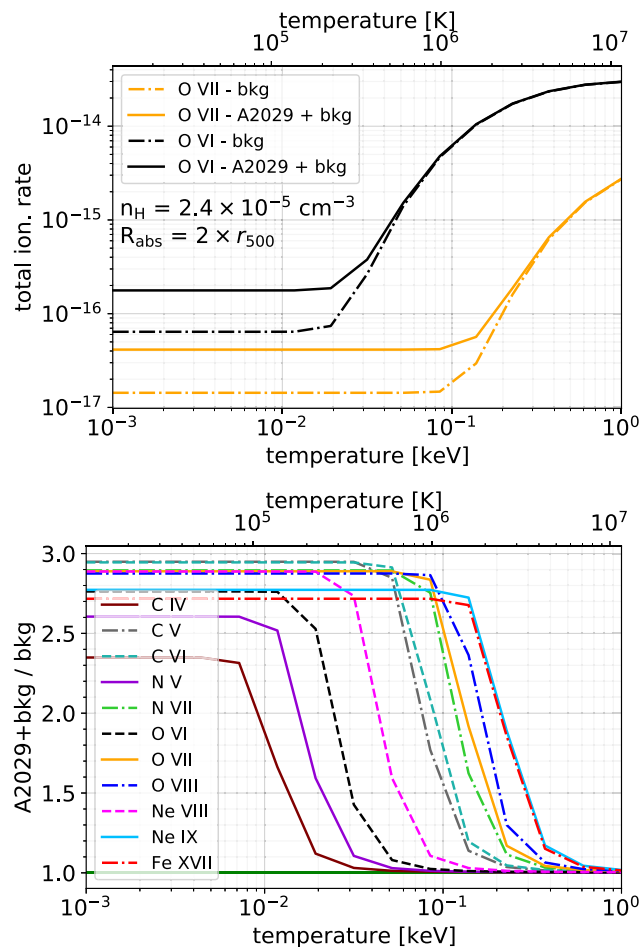
Figure 2. *Top panel:* The total ionization rate (number of ionizations per second per ion) plotted as a function of photoionized plasma temperature for O VI and O VII. The dash–dotted lines represent the total ionization rate for the Faucher-Giguère (2020) cosmic background at the redshift of cluster A2029 ($z = 0.0779$). The solid lines represent the total ionization rate if the SED of A2029 plus the Faucher-Giguère (2020) background is taken into account. The distance of the photoionized gas from the cluster center is $2 \times r_{500}$ and the hydrogen number density is set to 2.4×10^{-5} cm^{-3}. *Bottom panel:* Ratio of the total ionization rate for A2029 + *bkg* (solid lines in the top panel) and only the background *bkg* (dash–dotted lines in the top panel) for a representative set of UV and X-ray ions.

the cluster emission to the total ionization rate decreases. At high temperatures, the plasma is in its CIE limit and the addition of the cluster emission does not have any effect on the total ionization rate. The total photoionization rate does not change as a function of kT, but it increases by a factor of few if A2029 is added to the background spectrum (e.g. by a factor of 2.8 for O VI and a factor of 2.9 for O VII). Since the WHIM gas may not always reach temperatures sufficiently high to be fully in CIE, taking into account the photoionization from the galaxy cluster is important, mainly at lower gas temperatures, and should not be neglected.
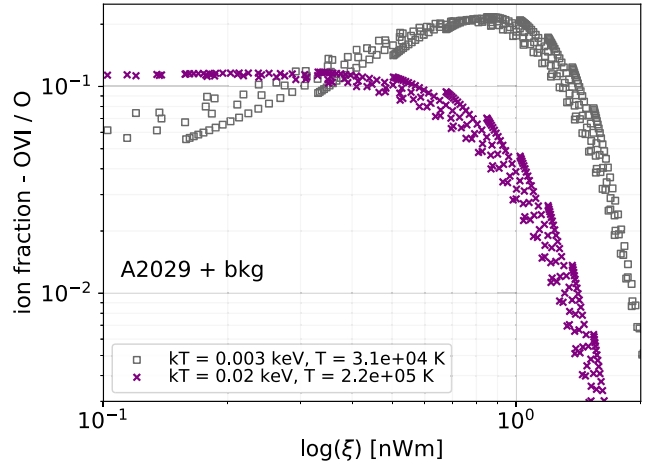
To study the behaviour with the hydrogen number density, we compare plasmas close to the temperature of the CIE temperature peak ($kT \approx 0.2$ keV) of O VII, and approximately 10 times lower than that ($kT \approx 0.02$ keV). The total photoionization rate does not change either with density, or with temperature (the photoionization cross-section is a constant with temperature and density), it only changes with the distance to the cluster.

Figure 4. Ion fraction of O VI as a function of the ionization parameter ξ for two chosen temperatures: 2.2×10^5 K (CIE peak temperature) and 3.1×10^4 K for a subset of distances R_{abs} and densities n_H selected in our studies. The figure illustrates how multiple ion fraction values are possible for a fixed value of ξ as a consequence of including photoionization by the SED of A2029 + *bkg*.

Figure 3. The total ionization rate (number of ionizations per second per ion) plotted as a function of hydrogen number density for O VI and O VII. The dash–dotted lines represent the total ionization rate for the Faucher-Giguère (2020) cosmic background at the redshift of cluster A2029 ($z = 0.0779$). The solid lines represent the total ionization rate if the SED of A2029 plus the Faucher-Giguère (2020) background is taken into account. The distance of the photoionized gas from the cluster center is $2 \times r_{500}$. In the top panel, we show plasma with temperature 0.02 keV (close to the CIE peak temperature of O VI) and in the bottom panel we show plasma with temperature 0.23 keV (close to the CIE peak temperature of O VII).

The total ionization rates, plotted in Fig. 3, increase with density because of the increasing contribution from collisional ionization; however, the details again depend on the temperature and the ion we study. As we see in the top panel of Fig. 3, at temperature 0.02 keV the total ionization rate of O VI is higher for A2029 + *bkg* in comparison with the background for densities $n_H < 10^{-3}$ cm^{-3}. As the density increases, the curves for A2029 + *bkg* and *bkg*-only converge to the same value. However, for O VII, the temperature is too low for collisional ionization to contribute and all the ionizations come from photoionization, which in this case is the same as when we described the behaviour of the photoionization rate. For the higher temperature of ≈ 0.2 keV (bottom panel of Fig. 3), the addition of the cluster emission can generally be neglected.

In equation (6), we defined the ionization parameter ξ. As already mentioned in Section 2.5, it often suffices to parametrize the ionization balance with this ionization parameter and the temperature. However, in the model where we include the light from the cluster as well as the ionizing background, the ionization balance can no

longer be parametrized solely with ξ and temperature T, but needs to be expressed as a function of (n_H, R_{abs}, T). We demonstrate this behaviour in Fig. 4, where we plot ion fractions of O VI as a function of the ionization parameter ξ for all n_H and R_{abs} values we used for the calculations and for two different temperatures. As Fig. 4 clearly shows, at a fixed value of ξ, many values of the ion fractions of O VI are possible. The spread of possible values then depends on the density n_H of the ionizing plasma and the distance R_{abs} from the ionization source as well as its temperature kT.

3.1.2 The effect of the additional cluster emission on the ionization balance

In Figs 5 and 6, we show how ion fractions of different ions (C IV, C V, C VI, N VII, Ne VIII, Ne IX, O VI, O VII, O VIII, Fe XVII) change as a function of temperature and the distance from the ionization source (A2029 + *bkg*) and compare the results with the ion fractions calculated for the case when the ionization source is only the UV/X-ray background (*bkg*, green solid line). We plot these ion fractions for density $n_H = 2.4 \times 10^{-5}$ cm^{-3}. For each distance in Figs 5 and 6, Table 2 lists a value of the ionization parameter ξ as well as the dimensionless ionization parameter for hydrogen U, defined as the ratio of the ionizing photon flux (in photons per unit area per unit time) to cn_H, where c is the speed of light and n_H is the total hydrogen number density (Davidson & Netzer 1979). In SPEX, this parameter is calculated from the SED and the ionization parameter ξ.

We can see that depending on temperature, the green line representing the results of the background SED (without the contribution of the cluster) forms an upper or lower boundary for the ion fractions. Other lines with different colours represent the ion fractions for the A2029 + *bkg* SED for different distances from the cluster centre. In grey, we show the distances that are smaller than r_{200} of A2029.[5] The temperature at which the background SED fractions transition from

---

[5]We use the scaling relation $r_{200} \approx (3/2)r_{500}$, which is approximately 2.04 Mpc for A2029.
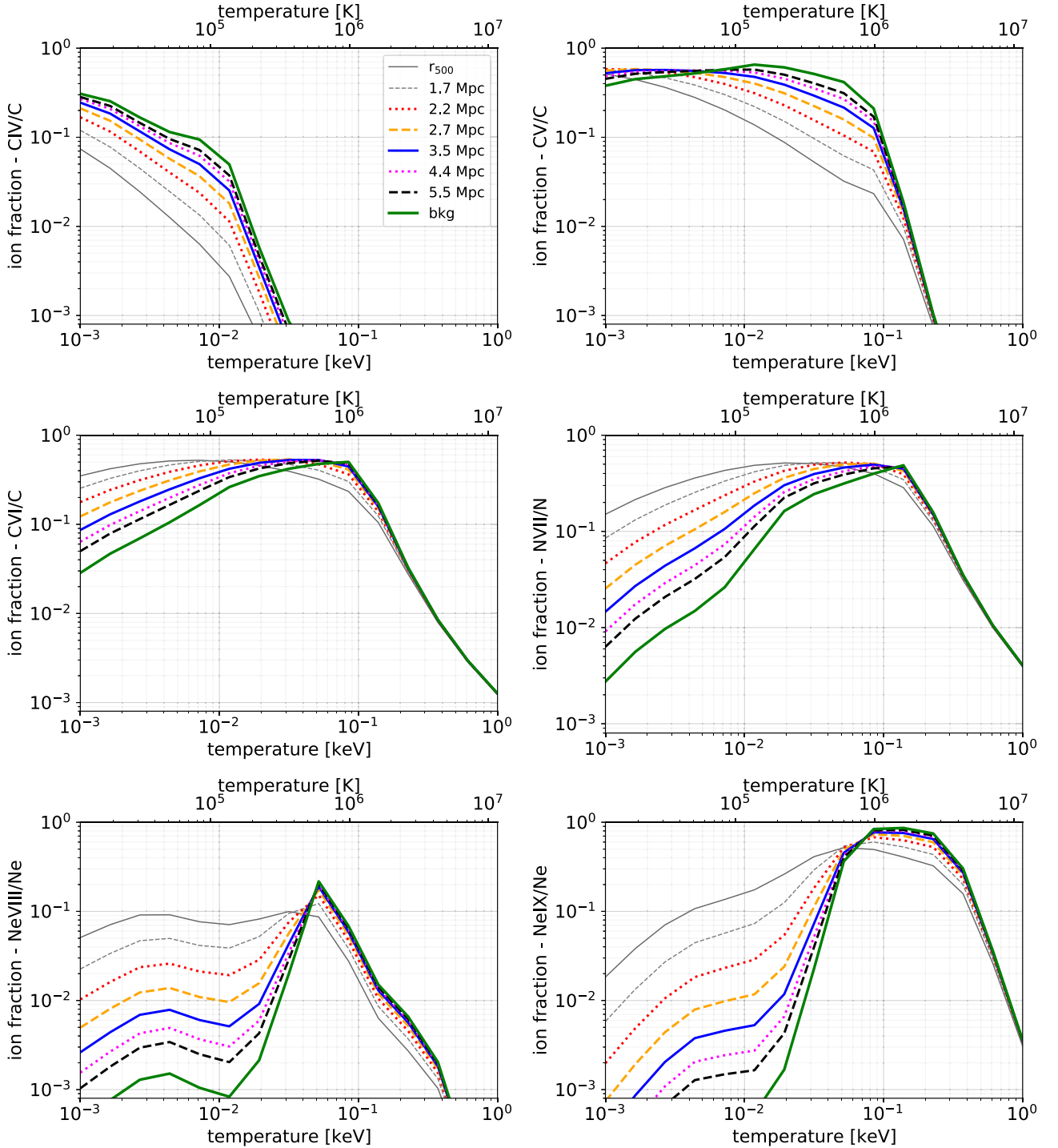
Figure 5. Ion fractions of C IV, C V, C VI, N VII, Ne VIII, and Ne IX as a function of plasma temperature for A2029 + *bkg* and the cosmic X-ray/UV background by Faucher-Giguère (2020). Different colours represent ion fractions for different distances from the cluster center as indicated in the legend and the green solid line shows the ion fractions for only the background. The hydrogen number density is assumed to be 2.4×10^{-5} cm^{-3}. The ionization parameters *U* and ξ which correspond to distances shown in this plot are listed in Table 2.

a lower to an upper limit is different for different ions. Depending on the temperature we also see that for some ions the differences between the A2029 + *bkg* and *bkg* can exceed an order of magnitude (see e.g. O VII, O VIII).

The ion fractions and the effect of the additional emission from the cluster photons also depend on the density of the plasma as well as the distance from the cluster. Therefore, we plot the ion fractions

as a function of the distance to the cluster, colour coded by the hydrogen number density in Fig. 7, and choose O VI and O VII ions as examples. In the collisional ionization equilibrium (dashed black line), the ion fractions depend only on temperature and do not change with distance, nor density of the gas.

Fig. 7 shows the ion fractions of O VI and O VII for two different temperatures: the peak temperature in CIE (left-hand panels), and a
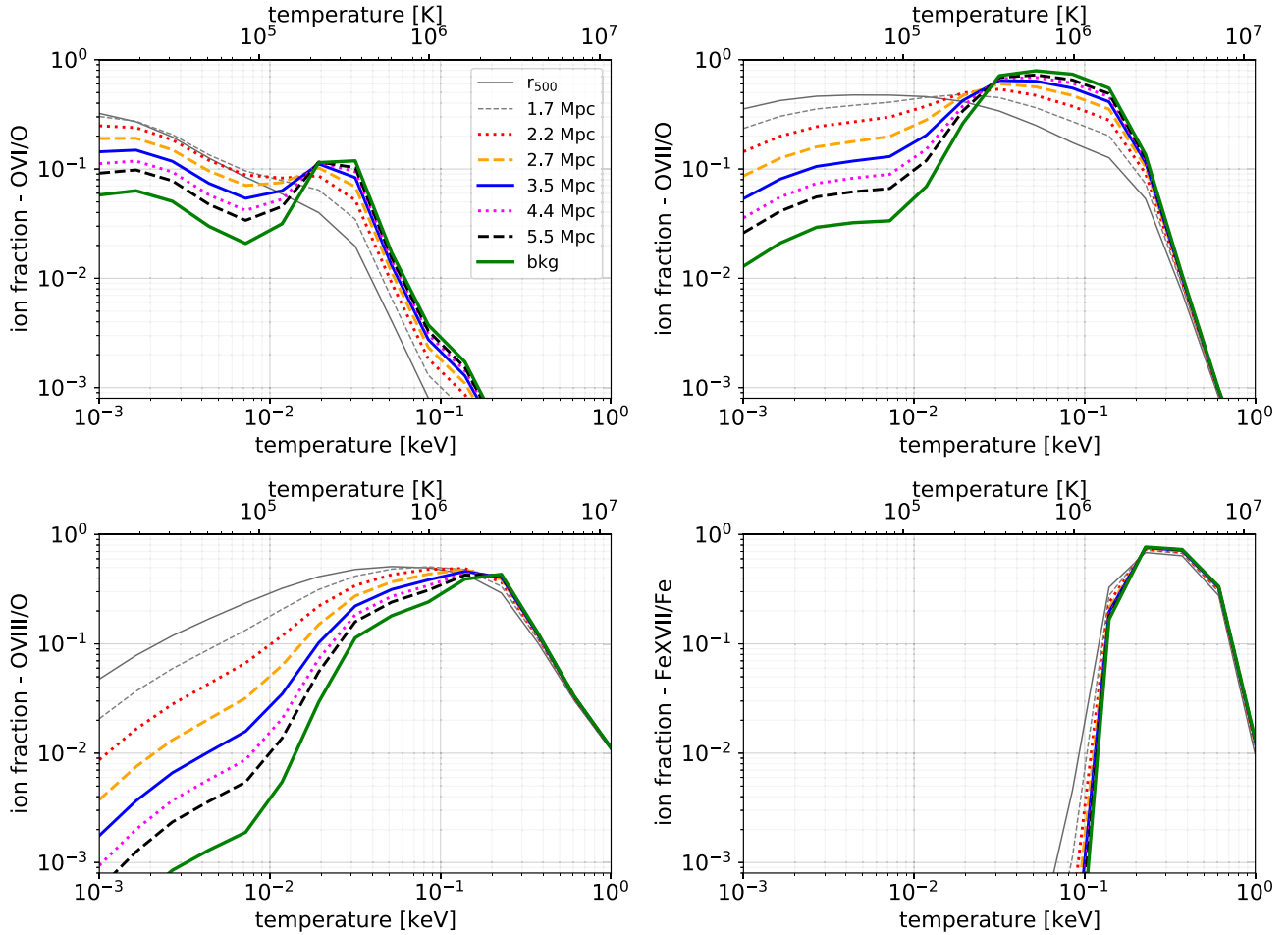
Figure 6. Same as Fig. 5 but for O VI, O VII, O VIII, and Fe XVII.

temperature 10 times lower (right-hand panels). Coloured solid lines represent the ion fractions of O VI and O VII for A2029 + *bkg*. All the lines asymptote to the ion fractions for the UV/X-ray background. In this plot, the background would be represented by horizontal lines, where the value would be a constant close to the values where the solid lines flatten towards larger distances.

One can, however, argue that gas at densities as low as 10^{-6} cm^{-3} is unlikely to exist at a distance of r_{500} from the cluster centre. Therefore, we calculate how the hydrogen number density is expected to change as a function of distance from the cluster using a theoretical curve from Walker et al. (2013) (their equation 20 without scaling factors). This curve can be expressed as

$$n_{\mathrm{H}}(r) = \frac{1}{1.2} [P(r)]^{3/5} [K(r)]^{-3/5}, \qquad (7)$$

where $P(r)$ and $K(r)$ are the pressure and entropy profiles, respectively. Within r_{200} the cluster is virialized and we can assume that the universal pressure profile $P(r)$ follows a generalized Navarro–Frenk–White (GNFW) profile as proposed by Nagai, Kravtsov & Vikhlinin (2007) (in this paper, we use parameters taken from Planck Collaboration 2013) and that the entropy profile $K(r)$ follows a power law as described in Pratt et al. (2010). For all distances $r \leq r_{200}$, we indicate the densities that fall below the theoretical prediction with dotted lines in Fig. 7.

We see that depending on the temperature, the ion fractions can differ significantly (by more than a factor of 10) if cluster emission is

Table 2. Distance R_{abs}, ionization parameter ξ, which is defined in equation (6), and ionization parameter for hydrogen U (defined in Section 3.1.2).

R_{abs} (Mpc)	$\log(\xi)$ (10^{-9} Wm)	U ($\times 10^{-2}$)
r_{500}	0.87	4.20
1.7	0.70	3.59
2.2	0.56	3.22
2.7	0.45	3.00
3.5	0.36	2.86
4.4	0.29	2.77
5.5	0.24	2.72
bkg	0.14	2.63

taken into account. Depending on the plasma properties and the species, the ion fractions can be higher or lower in comparison with the ionization by the background. For the temperatures close to the CIE peak, the *bkg* model behaves as an upper limit on the ion fractions, however, if we consider a lower temperature, this only holds true for lower densities while for higher densities the background model acts as a lower limit on the ion fractions instead. Fig. 7 also shows how the effect of photoionization by the galaxy cluster emission is stronger for smaller distances from the galaxy cluster and the difference between A2029 + *bkg* and only the background decreases towards larger distances. In our calculations,
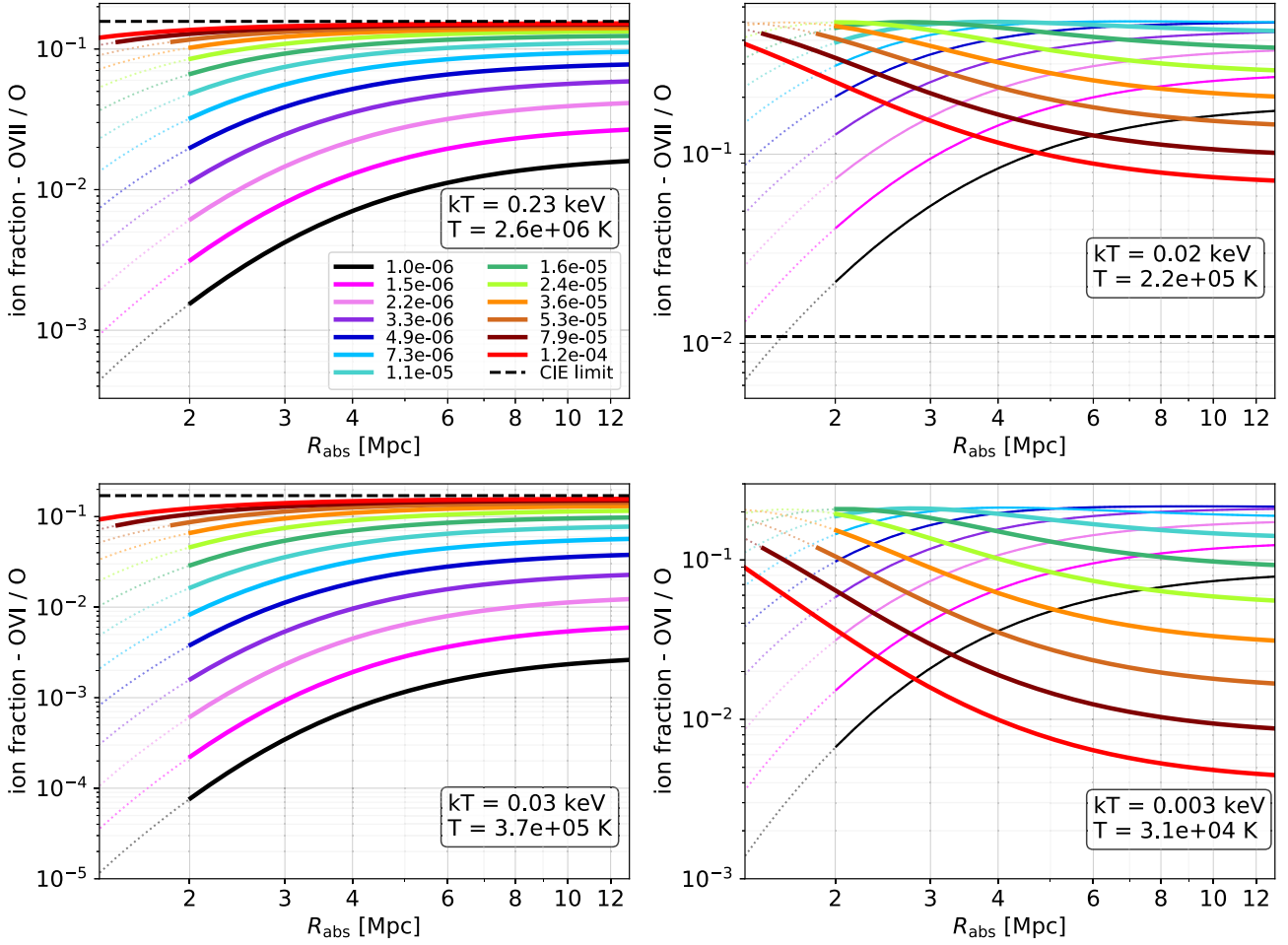
Figure 7. Ion fractions of O VII (top row) and O VI (bottom row) as a function of distance R_{abs} colour coded by the hydrogen number density in units of cm^{-3}. Coloured solid lines account for photoionization by the cluster A2029 and the background, the black dashed line shows O VI and O VII ion fractions in CIE. Left-hand panels show temperatures, for which the O VI and O VII ion fractions peak in CIE, right-hand panels show temperatures 10 times lower. Values that do not satisfy the conditions described in Section 3.1.2 are shown by dotted lines.

the difference between these two models was negligible for distances larger than 13 Mpc.

3.2 Comparison to A262 and A1795

Fig. 8 shows the same calculation as in the top panel of Fig. 2 for O VI (black lines) and O VII (orange lines) with the addition of the less massive clusters A1795 (dashed line) and A262 (dotted line). We see that less massive galaxy clusters have a smaller impact on the photoionization of nearby WHIM compared to more massive clusters.

More quantitatively, let us focus on the O VII ion fractions as an example. For A2029, the biggest differences between the SED of cluster + *bkg* and *bkg* only are seen for a WHIM temperature $kT = 0.23$ keV and density 10^{-6} cm^{-3} (black line in Fig. 7, top left panel). In this case, at r_{200} the ion fractions for A2029 + *bkg* in comparison with *bkg*-only differ by 162 per cent. At the distance of 5 Mpc, this difference drops to 52 per cent, and for distances bigger than 8 Mpc the difference is approximately 17.4 per cent. If we do the same comparison for A262, the differences between ion fractions of O VII drop to 90 per cent (at r_{200}), 4.5 per cent (at 5 Mpc), and 3.1 per cent (at 8 Mpc).
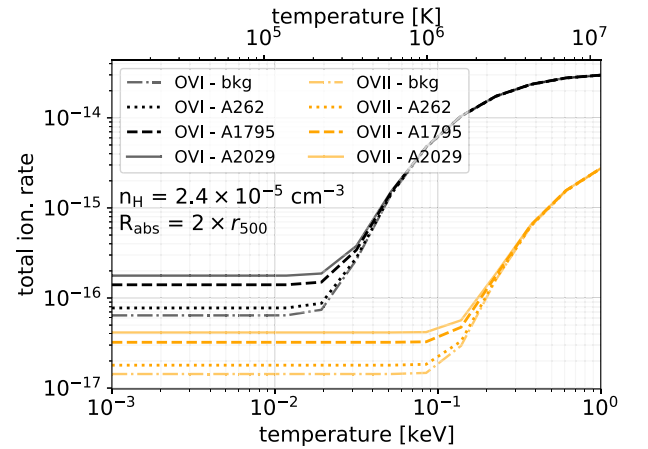
Figure 8. Same as the top panel of Fig. 2 but for ionization by the background (dash–dotted lines) and by the background plus A2029 (solid lines), A1795 + *bkg* (dashed lines), and A262 + *bkg* (dotted lines). Black lines show the total ionization rate for O VI, orange lines show O VII. The distance of the photoionized gas from the cluster centre is $2 \times r_{500}$ and the hydrogen number density is assumed to be 2.4×10^{-5} cm^{-3}.

In conclusion, the less massive clusters have lower luminosities, and therefore the change in ionization parameter ξ (between *bkg*-only and cluster + *bkg*) is also smaller. They, however, still alter the ionization balance and cause a similar effect as we described in Section 3.1. More generalized conclusions are difficult to provide since the ionization balance is a function of five parameters: density and temperature of the photoionized gas, distance of the photoionized gas form the galaxy cluster/group core and the cluster/group mass, and last but not least redshift as well. However, our research suggests that, if WHIM signals are detected in the future in the vicinity of massive clusters of galaxies, the effect of photoioinization from the cluster itself should be modelled carefully.

4 DISCUSSION

As we already mentioned in Section 2.5, due to the addition of the cluster emission, the ionization balance can no longer be parametrized by the ionization parameter ξ and the temperature of the photoionized plasma, but it needs to be expressed as a function of the density, temperature, *and* distance of the photoionized plasma to the galaxy cluster.

In this section we discuss two applications where this behaviour can be demonstrated: firstly, we calculate the column densities of a large scale structure WHIM filament using a toy model in Section 4.1 and secondly, we show how the cooling rates are suppressed in Section 4.2.

4.1 Impact on the predicted column densities

In this section, we consider a filament and calculate the column densities for two different orientations: (a) when the line of sight (LoS) is parallel to the spine of the filament and (b) when LoS is perpendicular to the spine of the filament. In both scenarios, we use A2029 as a cluster emission source and assume the filament has the shape of a cylinder. We describe the problem in cylindrical coordinates, where z is parallel to the spine of the filament.

In general, we calculate the ionic column density by integrating the ion number density (for a specific orientation) expressed as

$$n_i(r, z) = \frac{Y_i}{Y}(T, n_H, R_{abs}(r, z)) \times 0.3\,Z_\odot \times \rho(r) \times \frac{X_H}{m_p}, \qquad (8)$$

where $Y_i/Y = Y_i/Y(T, n_H, R_{abs}(r, z))$ are the ion fractions as calculated in Section 3 (e.g. O VII/O), $\rho(r)$ is the density of the photoionized plasma, m_p is the mass of a proton, and the hydrogen mass fraction X_H is set to 0.752. The metallicity is set to 0.3 $Z_\odot$, where $Z_\odot$ is the solar metallicity taken from Lodders et al. (2009) (since we calculate the column density of O, Ne, and C, this means that $Z_\odot$ = [O/H]$_\odot$ = $10^{8.76}/10^{12}$ for oxygen, $Z_\odot$ = [Ne/H]$_\odot$ = $10^{8.05}/10^{12}$ for neon and $Z_\odot$ = [C/H]$_\odot$ = $10^{8.39}/10^{12}$ for carbon). For both orientations (parallel and perpendicular), we select two different sets of densities and temperatures according to phase diagrams from the EAGLE cosmological simulations (Schaye et al. 2015) shown in Wijers et al. (2019): n_H = 10^{-6} cm^{-3} and T = 10^5 K and n_H = 10^{-5} cm^{-3} and T = $10^{5.5}$ K. We also consider a density typical for CGM gas: n_H = 10^{-4} cm^{-3} and T = $10^{6.5}$ K. For simplicity, we set the temperature and density of the filament to constant values in both chosen orientations.

In the first scenario, the LoS is parallel to the spine of the filament and centred on the galaxy cluster core. We calculate the column density (in a pencil beam) of O VI, O VII, O VIII, C V, and Ne VII by integrating the ion number density n_i as expressed in equation (8) along the coordinate z from r_{200} to r_{200} + 20 Mpc, where 20 Mpc is

our chosen length of the filament. We note that the filament length is still a point of discussion. For example, the maximum filament spine length found in the EAGLE simulation by Tuominen et al. (2021) is $\approx$35 Mpc, while Tanimura et al. (2020) report a range of filament lengths between 30 and 100 Mpc, which is not surprising given that the EAGLE simulation box is only 100 Mpc on a side. Malavasi et al. (2020) shows a distribution of filament lengths between 0 and 100 Mpc obtained from the galaxy distribution using SDSS measurements.

In the second scenario, the LoS is perpendicular to the spine of the filament and located at a distance of $z = 2 \times r_{500}$ from the centre of A2029. In this scenario, we integrate equation (8) along the r coordinate from zero to the Jeans length R_{Jeans}, which is an indicative size for overdense absorbers in any given line of sight (Schaye 2001). We set the mean molecular weight to $\mu = 0.625$. Columns 2 and 3 in Table 3 show the total and ionic column densities for the parallel orientation, columns 4 and 5 show the column densities for the perpendicular orientation. Column 6 shows the column densities for CGM-like properties of the studied gas, equally assuming the depth along the line of sight to be the Jeans length. For each ion, we compare the ionic column densities for gas exposed to A2029 + *bkg* and to only the background.

We see that in most of the cases, the addition of the cluster emission to the X-ray/UV background reduces the column densities. The biggest changes are seen for densities 10^{-6} and 10^{-5} cm^{-3} and can be up to almost factor of 5 (O VI). However, in the case of O VIII and Ne VIII, we see an enhancement of column densities, which can be 15–20 per cent for the parallel orientation, and 60–70 per cent for the perpendicular orientation (for these ions the biggest enhancements are seen for the density $n_H = 10^{-5}$ cm^{-3}).

The results of our toy model show that the changes in column densities are bigger for the perpendicular orientation, and in the case of parallel orientation, these changes do not exceed 50 per cent. This is, however, dependent on the length of the filament. If we reduce this length to 10 Mpc from 20 Mpc, the difference between A2029 + *bkg* and *bkg* is almost twice as large.

The detection of the effect reported in our studies can be challenging with current X-ray missions, however, not impossible. The column densities, currently reported in the literature are approximately of the order of 10^{15} cm^{-2}, more specifically, $N_{O VII} = (1.4 \pm 0.4) \times 10^{15}$ cm^{-2} (Kovács et al. 2019); $N_{O VIII} \sim 9.5 \times 10^{15}$ cm^{-2} (Fang et al. 2002b); Williams et al. (2007) provides measurements for a set of different ions: $N_{C V} \sim 10^{15.22}$ cm^{-2}, $N_{C VI} \sim 10^{15.16}$ cm^{-2}, $N_{O VII} \sim 10^{16.09}$ cm^{-2}, $N_{O VIII} \sim 10^{15.80}$ cm^{-2}, $N_{Ne IX} \sim 10^{15.83}$ cm^{-2}, $N_{N VI} < 10^{15.39}$ cm^{-2}, $N_{N VII} < 10^{15.39}$ cm^{-2}, and $N_{O V} \sim (10^{13.59}$–$10^{14.06})$ cm^{-2}. Ahoranta et al. (2020) report column densities of Ne IX and O VIII to be $N_{Ne IX} \sim 10^{15.4}$ cm^{-2} and $N_{O VIII} \sim 10^{15.5}$ cm^{-2}, respectively. All of these measurements probe WHIM in absorption against bright point-like sources, which would be a suggested method for the detection of the photoionization of WHIM by galaxy clusters, as reported in this paper. As we can see from Table 3, our reported column densities that have the biggest differences between cluster + *bkg* and *bkg* are typically of the same order or slightly lower than the column densities currently observed with the X-ray or UV missions. Nicastro, Fang & Mathur (2022) show that the Athena X-IFU will be able to probe absorbing column densities down to $N_{O VII} \sim 1.6 \times 10^{15}$ cm^{-2}, before problems related to systematic uncertainties on the continuum level become important. A few of the scenarios/geometries listed in our Table 3 can be probed with this limiting sensitivity. However, in order to access the typical column densities where the cluster photoionization has the largest effect ($N_{O VII} \sim$ a few of 10^{14} cm^{-2}, see column 4 of Table 3), grating

Table 3. Total column densities of hydrogen, oxygen, carbon, and neon, and ionic column densities of O VI, O VII, O VIII, C V, and Ne VIII for a toy model of a cosmic filament oriented parallel (columns 2 and 3) and perpendicular (columns 4 and 5) at a distance of $2 \times r_{500}$ to the line of sight as described in Section 4.1 for gas exposed to the SED of the background compared to the SED of A2029 + *bkg*. Column 6 shows the column densities for CGM-like properties of the studied gas, equally assuming the depth along the line of sight to be the Jeans length. For the parallel orientation, the length of the filament is assumed to be 20 Mpc, and for the perpendicular orientation its thickness is the Jeans scale. If the column densities for the background and A2029 + *bkg* differ by more than a factor of 2, we highlight them in the bold face.

A2029	Parallel orientation		Perpendicular orientation		CGM
$n_{\rm H}$ (cm^{-3})	10^{-6}	10^{-5}	10^{-6}	10^{-5}	10^{-4}
T (K)	10^5	$10^{5.5}$	10^5	$10^{5.5}$	$10^{6.5}$
kT (keV)	0.009	0.03	0.009	0.03	0.27
$R_{\rm Jeans}$ (Mpc)	3.34	1.88	3.34	1.88	1.88
$N_{\rm H}$ (cm^{-2})	6.17×10^{19}	6.17×10^{20}	1.03×10^{19}	5.79×10^{19}	5.79×10^{20}
$N_{\rm O}$ (cm^{-2})	1.07×10^{16}	1.07×10^{17}	1.78×10^{15}	1.00×10^{16}	1.00×10^{17}
$N_{\rm C}$ (cm^{-2})	4.54×10^{15}	4.54×10^{16}	7.59×10^{14}	4.27×10^{15}	4.27×10^{16}
$N_{\rm Ne}$ (cm^{-2})	2.08×10^{15}	2.08×10^{16}	3.47×10^{14}	1.95×10^{15}	1.95×10^{16}
$N_{\rm O\,VI}^{\rm A2029+bkg}$ (cm^{-2})	2.33×10^{14}	7.64×10^{15}	$\mathbf{1.10 \times 10^{13}}$	$\mathbf{3.42 \times 10^{14}}$	4.11×10^{13}
$N_{\rm O\,VI}^{bkg}$ (cm^{-2})	2.95×10^{14}	8.68×10^{15}	$\mathbf{4.93 \times 10^{13}}$	$\mathbf{8.15 \times 10^{14}}$	4.24×10^{13}
$N_{\rm O\,VII}^{\rm A2029+bkg}$ (cm^{-2})	3.19×10^{15}	6.47×10^{16}	$\mathbf{2.75 \times 10^{14}}$	4.48×10^{15}	1.45×10^{16}
$N_{\rm O\,VII}^{bkg}$ (cm^{-2})	3.67×10^{15}	6.85×10^{16}	$\mathbf{6.13 \times 10^{14}}$	6.43×10^{15}	1.52×10^{16}
$N_{\rm O\,VIII}^{\rm A2029+bkg}$ (cm^{-2})	5.02×10^{15}	2.81×10^{16}	8.44×10^{14}	4.18×10^{15}	4.44×10^{16}
$N_{\rm O\,VIII}^{bkg}$ (cm^{-2})	4.92×10^{15}	2.41×10^{16}	8.22×10^{14}	2.26×10^{15}	4.53×10^{16}
$N_{\rm C\,V}^{\rm A2029+bkg}$ (cm^{-2})	2.17×10^{14}	1.13×10^{16}	$\mathbf{1.53 \times 10^{13}}$	$\mathbf{0.43 \times 10^{15}}$	4.50×10^{13}
$N_{\rm C\,V}^{bkg}$ (cm^{-2})	2.72×10^{14}	1.33×10^{16}	$\mathbf{4.54 \times 10^{13}}$	$\mathbf{1.25 \times 10^{15}}$	4.58×10^{13}
$N_{\rm Ne\,VIII}^{\rm A2029+bkg}$ (cm^{-2})	2.30×10^{14}	11.35×10^{14}	2.49×10^{13}	$\mathbf{1.79 \times 10^{14}}$	1.37×10^{14}
$N_{\rm Ne\,VIII}^{bkg}$ (cm^{-2})	2.56×10^{14}	9.33×10^{14}	4.28×10^{13}	$\mathbf{0.88 \times 10^{14}}$	1.44×10^{14}

spectrometers with a higher resolving power and which can thus probe lower line equivalent widths robustly, are needed. Missions such as *Arcus* and *Lynx* would therefore be ideal, since their resolving power at 0.5 keV is 2500 and >5000, respectively. Let us take as an example a resonant line of O VII at 573.95 eV. Scaling from equations (4) and (13) of Nicastro et al. (2022), for an absorption against a bright Seyfert galaxy with flux of 1 mCrab, it would take *Arcus* approximately 500 ks and *Lynx/XGS* 50 ks to probe column densities of $N_{\rm O\,VII}^{\rm A2029+bkg} = 2.75 \times 10^{14}$ cm^{-2}. A detailed feasibility simulation is deferred to future work.

4.2 Suppression of cooling rates

In the case of CIE, when no external radiation is present, the cooling rates depend only on the temperature of the CIE plasma, but do not depend on its density after normalization by $n_e n_{\rm H}$. However, in the presence of the cluster, as we have shown in the previous sections, the normalized cooling rates also depend on a distance $R_{\rm abs}$ and a density $n_{\rm H}$.

The presence of the photoionizing radiation causes a suppression of the cooling rates in comparison with the CIE case (as described in Section 1). In Fig. 9, we show the total cooling in keV s^{-1} m^{-3} for the background SED (black dashed line) and for the SED of A2029 + *bkg* for two different distances: $2 \times r_{500}$ (purple solid line) and $3 \times r_{500}$ (orange solid line) for density $n_{\rm H} = 10^{-6}$ cm^{-3} and metallicities of $0.3 \times Z_\odot$, where similarly to Section 4.1, $Z_\odot$ is taken from Lodders et al. (2009). As expected, the total cooling rates are suppressed in comparison with only the background, and the closer we get to the cluster, the lower the total cooling rate
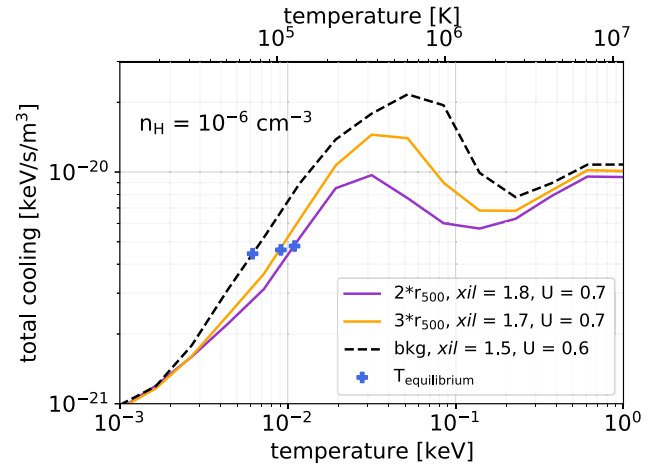
Figure 9. *Left-hand panel:* total cooling rate for the gas with density $n_{\rm H} = 10^{-6}$ cm^{-3} at distance $R_{\rm abs} = 2 \times r_{500}$ (purple solid line) and $R_{\rm abs} = 3 \times r_{500}$ (orange solid line). The dashed black line represents the total cooling rate for the SED of the background. The equilibrium temperature for each curve is marked by the blue plus sign. Parameter xil is defined as $xil = \log \xi$ in units of 10^{-9} Wm. The metallicity is set to 0.3 $Z_\odot$ for carbon up to nickel.

is. The biggest differences can be seen for temperatures of a few times 10^{-3} to 0.2 keV. The total cooling rates change at most by a factor of 3 for temperatures around 0.09 keV and densities around 10^{-6} cm^{-3}. When we check individual contributions to the total cooling, the biggest change between background and A2029 + *bkg* is in dielectronic recombination by almost a factor of 7 (at $kT =$

0.05 keV) and for collisional excitation by a factor of 6 (at $kT = 0.09$ keV).

Even though we see that the cooling rates are suppressed once the cluster emission is taken into account, it is also important to calculate on what time scales such cooling happens and whether this change could be relevant. For that we calculate the cooling time t_{cool} for the two most prominent cases from our column density calculations in Section 4.1: (a) $n_H = 10^{-6}$ cm^{-3}, $T = 10^5$ K, and (b) $n_H = 10^{-5}$ cm^{-3}, $T = 10^{5.5}$ K. The cooling time t_{cool} is expressed as

$$t_{cool} = \frac{3 n_{tot} k_B T}{2 n_{tot}^2 \Lambda} \, , \tag{9}$$

where $n_{tot} = n_i + n_e$ is the total particle number density of gas consisting of the sum of the ion number density n_i and the electron number density n_e, and Λ is the normalized cooling rate in keV m^{-3} s^{-1}. The denominator in equation (9) $n_{tot}^2 \Lambda$ then represents the total cooling rate of the gas in keV m^{-3} s^{-1} which we plot along the y-axis of Fig. 9.

In case (a), we obtain $t_{cool} = 255.5$ Gyr, and in case (b) $t_{cool} = 10.1$ Gyr. By comparing t_{cool} to the Hubble time (≈ 14.4 Gyr), we see that the suppression of cooling rates will not be important for the gas with density of 10^{-6} cm^{-3}, but can potentially affect gas with density of 10^{-5} cm^{-3}, when the cooling time is around 10 Gyr. We note, however, that in our calculations we do not include adiabatic cooling due to the Hubble expansion. The addition of cluster emission causes an increase in the thermal equilibrium temperature of approximately 38 per cent ($3 \times r_{500}$) or 56 per cent ($2 \times r_{500}$) for $n_H = 10^{-6}$ cm^{-3} in comparison with the *bkg* model.

If we increase the metallicity to $Z_\odot$ instead, which might be relevant for the CGM, the biggest differences can be seen again for temperatures of a few times 10^{-3} to 0.2 keV. The total cooling rates change by a factor of 5 for temperatures around 0.09 keV and densities around 10^{-6} cm^{-3}. When we check individual contributions to the total cooling, the biggest change between cooling for the *bkg* model and A2029 + *bkg* is in dielectronic recombination and collisional excitation by almost factor of 7 for both processes at the same temperature as for the metallicity $0.3 \times Z_\odot$. The addition of cluster emission causes an increase in equilibrium temperature of approximately 67 per cent ($3 \times r_{500}$) or 80 per cent ($2 \times r_{500}$) for $n_H = 10^{-6}$ cm^{-3} in comparison with the *bkg* model.

5 CONCLUSIONS

This paper studies the impact of the radiation emitted by the intracluster gas in galaxy clusters on their environment. In particular, we show how the addition of photons from galaxy clusters alters the ionization balance of the surrounding WHIM relative to models considering any photoionization by the cosmic UV and X-ray background.

We model the spectra of the intracluster gas from three different cool-core clusters (A262, A1795, and A2029) using the SPEX software package. These spectra, together with the emission from the cosmic UV/X-ray background, are used as ionizing sources for the photoionization model to realistically describe the WHIM. We examine the effect on the ionization balance for a set of densities and temperatures of the WHIM gas, as well as distances of the WHIM to the galaxy clusters (Section 3). In Section 4, we discuss the effect on the column densities for a toy model of WHIM filament and calculate how much the cooling rates are suppressed by adding the galaxy cluster to the ionizing source.

Due to the changing spectrum of the radiation that the absorbing gas receives at different distances from the galaxy cluster, the ionization balance can no longer be solely described as a function of the ionization parameter ξ and the temperature of the photoionized

gas. Instead, the ionization balance needs to be parametrized as a function of the temperature and density of the photoionized gas, as well as the distance to the galaxy cluster (Fig. 4).

We see that more massive clusters alter the ionization balance of the plasma in their vicinity more than the less massive clusters and cause bigger differences in the total ionization rate (Fig. 8).

Our main results can be summarized as follows:

(i) For massive, relaxed clusters such as A2029, the addition of the galaxy cluster emission to the UV and X-ray background emission increases the total ionization rate, especially in the regime of lower densities and temperatures, where photoionization dominates over collisional ionization (Figs 2 and 3).

(ii) The ion fractions obtained from the photoionization by the cosmic UV and X-ray background represent either an upper or lower limit (depending on the plasma properties) on the ion fractions calculated as a function of distance using the cluster + *bkg* emission as opposed to *bkg*-only emission (Figs 5 and 6).

(iii) The effect of the photoionization by cluster + *bkg* emission is strongest towards the galaxy cluster outskirts and decreases at larger distances from the cluster (Fig. 7). The differences between *bkg* and cluster + *bkg* are negligible for distances larger than 13 Mpc.

(iv) The addition of the galaxy cluster emission affects the column densities of our toy filament. For lines of sight passing close to the cluster outskirts, O VI can be suppressed by a factor of up to 4.5 ($n_H = 10^{-6}$ cm^{-3}) or a factor of 2.4 ($n_H = 10^{-5}$ cm^{-3}), O VII by a factor of 2.2 ($n_H = 10^{-6}$ cm^{-3}), C V by a factor of 3 (for both densities 10^{-6} and 10^{-5} cm^{-3}), and Ne VIII can be boosted by a factor of 2 ($n_H = 10^{-5}$ cm^{-3}) (Section 4.1 and Table 3).

(v) The addition of the cluster emission to the model suppresses the total cooling rates at maximum by a factor of 3 for the metallicities of $0.3 \times Z_\odot$, and by a factor of 5 for $Z_\odot$. In both cases, this change is most significant for temperatures ranging from a few times 10^{-3} to 0.2 keV (for a gas with $n_H = 10^{-6}$ cm^{-3}).

In conclusion, our work emphasizes that the impact of the cluster photoionization on the column densities should be considered when interpreting future detections of the IGM near galaxy clusters in absorption.

DATA AVAILABILITY

The data set generated and analysed during this study is available in the ZENODO repository (Štofanová et al. 2022).

REFERENCES

Ahoranta J. et al., 2021, A&A, 656, A107
Ahoranta J. et al., 2020, A&A, 634, A106
Babul A., White S. D. M., 1991, MNRAS, 253, 31P
Bristow P. D., Phillipps S., 1994, MNRAS, 267, 13
Cen R., Miralda-Escudé J., Ostriker J. P., Rauch M., 1994, ApJ, 437, L9

Cen R., Ostriker J. P., 1999, ApJ, 514, 1

Davé R. et al., 2001, ApJ, 552, 473

Davidson K., Netzer H., 1979, Rev. Mod. Phys., 51, 715

Dekel A., Rees M. J., 1987, Nature, 326, 455

Efstathiou G., 1992, MNRAS, 256, 43P

Fang T., Bryan G. L., Canizares C. R., 2002a, ApJ, 564, 604

Fang T., Marshall H. L., Lee J. C., Davis D. S., Canizares C. R., 2002b, ApJ, 572, L127

Fang T., Sembach K. R., Canizares C. R., 2003, ApJ, 586, L49

Faucher-Giguère C.-A., 2020, MNRAS, 493, 1614

Finoguenov A., Briel U. G., Henry J. P., 2003, A&A, 410, 777

Fujimoto R. et al., 2004, PASJ, 56, L29

Fukugita M., Hogan C. J., Peebles P. J. E., 1998, ApJ, 503, 518

Haardt F., Madau P., 2012, ApJ, 746, 125

Hellsten U., Gnedin N. Y., Miralda-Escudé J., 1998, ApJ, 509, 56

Kaastra J. S., Lieu R., Tamura T., Paerels F. B. S., den Herder J. W., 2003, A&A, 397, 445

Kaastra J. S., Mewe R., Nieuwenhuijzen H., 1996, in Yamashita K., Watanabe T., eds, UV and X-ray Spectroscopy of Astrophysical and Laboratory Plasmas. p. 411

Kaastra J. S., Raassen A. J. J., de Plaa J., Gu L., 2018, SPEX X-ray spectral fitting package, Zenodo

Kaastra J. S., Raassen A. J. J., de Plaa J., Gu L., 2020, SPEX X-ray spectral fitting package

Kovács O. E., Bogdán Á., Smith R. K., Kraft R. P., Forman W. R., 2019, ApJ, 872, 83

Krolik J. H., McKee C. F., Tarter C. B., 1981, ApJ, 249, 422

Kull A., Böhringer H., 1999, A&A, 341, 23

Lodders K., Palme H., Gail H. P., 2009, Landolt Börnstein, 4B, 712

Lynds R., 1971, ApJ, 164, L73

Malavasi N., Aghanim N., Douspis M., Tanimura H., Bonjean V., 2020, A&A, 642, A19

Martizzi D. et al., 2019, MNRAS, 486, 3766

Mehdipour M., Kaastra J. S., Kallman T., 2016, A&A, 596, A65

Nagai D., Kravtsov A. V., Vikhlinin A., 2007, ApJ, 668, 1

Nicastro F. et al., 2003, Nature, 421, 719

Nicastro F. et al., 2005a, Nature, 433, 495

Nicastro F. et al., 2005b, ApJ, 629, 700

Nicastro F. et al., 2018, Nature, 558, 406

Nicastro F., Fang T., Mathur S., 2022, preprint (arXiv:2203.15666)

Perna R., Loeb A., 1998, ApJ, 503, L135

Planck Collaboration V., 2013, A&A, 558, C2

Pratt G. W. et al., 2010, A&A, 511, A85

Quinn T., Katz N., Efstathiou G., 1996, MNRAS, 278, L49

Rasmussen A., Kahn S. M., Paerels F., 2003, in Rosenberg J. L., Putman M. E., eds, Astrophysics and Space Science Library, Vol. 281, The IGM/Galaxy Connection. The Distribution of Baryons at z = 0. Springer, Dordrecht, p. 109

Sargent W. L. W., Young P. J., Boksenberg A., Tytler D., 1980, ApJS, 42, 41

Schaye J. et al., 2015, MNRAS, 446, 521

Schaye J., 2001, ApJ, 559, 507

Shull J. M., Smith B. D., Danforth C. W., 2012, ApJ, 759, 23

Silk J., 1985, ApJ, 297, 1

Štofanová L., Kaastra J., Mehdipour M., de Plaa J., 2021, A&A, 655, A2

Štofanová L., Simionescu A., Wijers N. A., Schaye J., Kaastra J., 2022, Zenodo

Takei Y., Henry J. P., Finoguenov A., Mitsuda K., Tamura T., Fujimoto R., Briel U. G., 2007, ApJ, 655, 831

Tanimura H., Aghanim N., Kolodzig A., Douspis M., Malavasi N., 2020, A&A, 643, L2

Tarter C. B., Tucker W. H., Salpeter E. E., 1969, ApJ, 156, 943

Tepper-García T., Richter P., Schaye J., Booth C. M., Dalla Vecchia C., Theuns T., 2012, MNRAS, 425, 1640

Thoul A. A., Weinberg D. H., 1996, ApJ, 465, 608

Tumlinson J. et al., 2011, Science, 334, 948

Tumlinson J., Peeples M. S., Werk J. K., 2017, ARA&A, 55, 389

Tuominen T. et al., 2021, A&A, 646, A156

Vikhlinin A., Kravtsov A., Forman W., Jones C., Markevitch M., Murray S. S., Van Speybroeck L., 2006, ApJ, 640, 691

Virtanen P. et al., 2020, Nat. Methods, 17, 261

Walker S. A., Fabian A. C., Sanders J. S., Simionescu A., Tawara Y., 2013, MNRAS, 432, 554

Weinberg D. H., Miralda-Escudé J., Hernquist L., Katz N., 1997, ApJ, 490, 564

Werk J. K. et al., 2014, ApJ, 792, 8

Werner N., Finoguenov A., Kaastra J. S., Simionescu A., Dietrich J. P., Vink J., Böhringer H., 2008, A&A, 482, L29

Wiersma R. P. C., Schaye J., Smith B. D., 2009, MNRAS, 393, 99

Wijers N. A., Schaye J., 2022, MNRAS, 514, 5214

Wijers N. A., Schaye J., Oppenheimer B. D., Crain R. A., Nicastro F., 2019, MNRAS, 488, 2947

Williams R. J., Mathur S., Nicastro F., Elvis M., 2007, ApJ, 665, 247

Zappacosta L., Mannucci F., Maiolino R., Gilli R., Ferrara A., Finoguenov A., Nagar N. M., Axon D. J., 2002, A&A, 394, 7

Zhang Y., Anninos P., Norman M. L., 1995, ApJ, 453, L57

This paper has been typeset from a TEX/LATEX file prepared by the author.